Article

Embedded Real-Time Implementation of Bio-Inspired Central Pattern Generator with Self-Repairing Function

Jinda Xu [1], Meili Lu [2], Zhen Zhang [1] and Xile Wei [1,*]

[1] Tianjin Key Laboratory of Process Measurement and Control, School of Electrical and Information Engineering, Tianjin University, Tianjin 300072, China; xujinda@tju.edu.cn (J.X.); zhangz@tju.edu.cn (Z.Z.)

[2] School of Information Technology Engineering, Tianjin University of Technology and Education, Tianjin 300222, China; meililu@tute.edu.cn

[*] Correspondence: xilewei@tju.edu.cn

Abstract: Both robustness and self-repairing of the rhythmic behaviors generated by central pattern generators (CPGs) play significant roles in locomotion control. Although current CPG models have been established to mimic rhythmic outputs, the mechanisms by which the self-repairing capacities of CPG systems are formed are largely unknown. In this paper, a novel bio-inspired self-repairing CPG model (BiSRP-CPG) is proposed based on the tripartite synapse, which reveals the critical role of astrocytes in the dynamic coordination of CPGs. BiSRP-CPG is implemented on the parallel FPGA platform to simulate CPG systems on real physiological scale, in which a hardware implementation method without multiplier is utilized to break the limitation of FPGA hardware resources. The experimental results verified both the robustness and self-repairing capabilities of rhythm of BiSRP-CPG in the presence of stochastic synaptic inputs and "faulty" synapse. Under the synaptic failure rate of 20%, BiSRP-CPG suffered only 10.53% performance degradation, which was much lower than the 36.84% spike loss rate of CPG networks without astrocytes. This paper provides an insight into one of the possible self-repair mechanisms of brain rhythms which can be utilized to develop autonomously fault-tolerant electronic systems.

Keywords: astrocyte; robustness; self-repairing; Central Pattern Generator (CPG); Field-Programmable Gate Array (FPGA)

1. Introduction

Central pattern generators (CPGs) are the basis for rhythmic regulation of the motor nervous system, which have been proved to generate rhythmic motion patterns without sensory feedback and external input stimulus [1–6]. Under the control of the nerve center, the interneurons within the CPG generate self-oscillation through mutual inhibition and output phase-interlocked periodic signals [7]. The neuron environment of CPG may be affected by multiple unfavorable factors, such as noise, faults, etc. These adverse factors may result in varying degrees of system performance degradation. The ability to sense failures, classify failures, and implement corrective actions to maintain functional operation is a key requirement for CPG systems. For example, Tavoosi, J. et al., implemented robust PID control through an online-tuned fuzzy logic system to deal with dynamic disturbance [8]. Huang et al. solved the problems of actuator failures and perturbations in a stochastic nonlinear system via fuzzy neural networks [9]. Cao et al. realized the 3D motion of the fish robot with an improved phase oscillator, and verified the stability and robustness of the proposed CPG system in experiments [10,11]. Therefore, it is worthwhile to investigate the factors affecting the robustness and self-repairing capabilities of CPG output.

In this paper, the mechanism of CPG stability and fine repair ability was studied based on the real physiological environment. We hypothesized that astrocyte-mediated environment is the key for the CPG network to acquire stability and self-repairing capacity. Astrocytes are a type of glial cells distributed in the central and peripheral nervous

systems, which not only participate in the modulation of synaptic formation, but can also dynamically regulate the excitability of neurons and produce neurotransmitters [12–15]. More importantly, astrocytes have been demonstrated to play a crucial role in the robustness and self-repairing mechanism of neural networks [16–18]. The gatekeeper Nadkarni and Jung model described the interaction of astrocytes and neurons via the tripartite synapses [19]. The astrocyte-mediated indirect feedback signaling pathway endows the postsynaptic terminals with the ability to transmit signals to presynaptic terminals. This process can modulate the synaptic transmission probability of release (PR), thereby exerting the self-repairing function [20]. Inspired by this, the authors mimicked the robustness and self-repairing capabilities of tripartite synapses to provide reliability for the CPG systems.

This paper proposes a novel astrocyte-mediated CPG model based on the Komendantov–Kononenko (K-K) neuron model and the tripartite synaptic self-repairing model to capture the robustness and self-repairing capabilities of rhythmic output [21,22]. The simulation results demonstrate that the modulation of synaptic activities by the astrocyte–neuron system plays a crucial role in stabilizing CPG rhythmic output and self-repair of its abnormal rhythm. In addition, due to the increasing complexity of the model, traditional software simulation methods always require massive operating consumption and long computing time, which makes it challenging to achieve real-time and parallel simulation. Therefore, we realized the real-time simulation of the CPG network based on the FPGA hardware platform, solved the contradiction between model complexity and simulation cost, and built a visualization research platform more similar to the biological neural network.

The rest of this paper is organized as follows: Section 2 presents the self-repair mechanism of astrocytes. In Section 3, we provide the bio-inspired self-repairing CPG model (BiSRP-CPG). Section 4 explains the robustness of the BiSRP-CPG model and demonstrates the self-repair mechanism from synaptic dynamics. Hardware implementation and results are discussed in Section 5. Some critical issues and further improvements are discussed in Section 6.

2. Background and Relative Works

Astrocytes can encapsulate more than 10^5 synapses and closely link to adjacent neurons, thereby regulating the action patterns of neurons [23,24]. The mechanism of interaction between astrocytes and CPG neurons is provided in Figure 1. When an action potential is delivered to the presynaptic terminal, it stimulates the presynaptic neuron to release glutamate, causing the postsynaptic neuron to depolarize. Subsequently, 2-arachidene glycerol (2-AG) is synthesized and released from the postsynaptic neuron. Since there are 2-AG receptors on both the presynaptic terminal and astrocytes, there are two feedback pathways of 2-AG. The first is direct feedback: part of the 2-AG binds directly to the receptors on the presynaptic terminal, causing a decrease in the synaptic transmission PR, called depolarization-induced suppression of excitation (DSE) [25]. The second is indirect feedback: the remainder of the 2-AG binds to the receptors on astrocytes and stimulates the release of IP3 inside the astrocytes. The binding of IP3 with its receptors on the endoplasmic reticulum (ER) opens channels that trigger a transient wave of Ca^{2+} [26]. Subsequently, astrocytes release glutamate and transmit information to presynaptic neurons in the indirect feedback pathway. This process increases the PR, which is called endocannabinoid-mediated synaptic potentiation (eSP) [27]. This astrocyte-mediated tripartite synapse CPG model enables synaptic modulation in the presence of random synaptic inputs and "fault" synapses, which is the key process in the self-repairing mechanism.
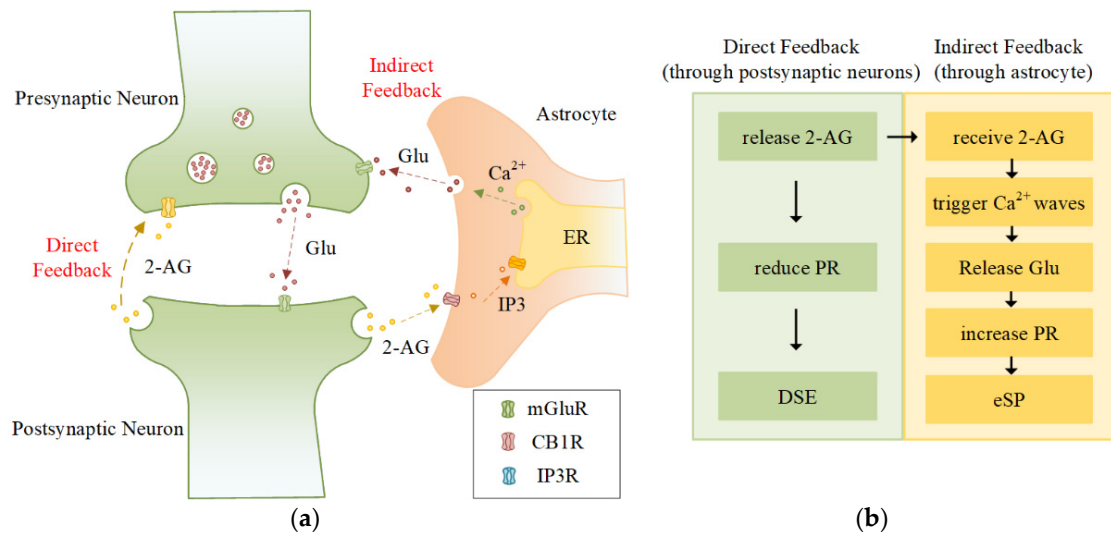
Figure 1. (**a**) The astrocyte-mediated tripartite synapse model (adapted with permission from Ref. [28]. 2018, Liu, J); (**b**) Simplified functional diagram of tripartite synaptic.

3. Materials and Methods

3.1. Neuron Model

This paper implemented a minimal CPG network constructed by K-K neuron models to capture the self-repairing mechanism. The K-K model contains a fast membrane potential variable and seven slowly varying variables described by first-order differential equations [21]. Eight conductance-based ionic currents were obtained from this model, including the TTX-sensitive sodium current, the stationary voltage-dependent sodium current, the leaky sodium current, the TEA-sensitive potassium current, the leaky potassium current, the inward calcium current, the stationary voltage-dependent calcium current, and the voltage-dependent outward current. In additional, the synaptic model proposed by Jorge Golowasch was utilized to simulate the coupling of two K-K neurons in the CPG network [29], which can be obtained as

$$I_{syn} = g_{prepost} \left(V_{post} - E_{syn} \right) / \left(1 + \exp \left(s_{fast} \left(V_{fast} - V_{pre} \right) \right) \right) \tag{1}$$

where $g_{prepost}$ is the maximal synaptic conductance between neurons; V_{post} and V_{pre} are the membrane potentials of presynaptic and postsynaptic neurons, respectively; $E_{syn} = -65$ mV is the reversal synaptic potential; and $V_{fast} = 44.7$ mV determines the graded synaptic threshold.

3.2. Tripartite Synapse Model

Wade et al. systematically proposed the tripartite synaptic model with astrocytes; this paper followed this model for theoretical analysis and hardware implementation [22]. The description of the tripartite synapse model is as follows. When an action potential reaches the synapse, it causes the postsynaptic neuron to depolarize and release 2-AG, as described by [22]:

$$\frac{dAG}{dt} = (-AG)/\tau_{AG} + r_{AG}d(t - t_{sp}), \tag{2}$$

where AG is the value of the released 2-AG, τ_{AG} is the 2-AG decay rate, r_{AG} is the 2-AG production rate, and tsp is the time of the postsynaptic spike. When the 2-AG reaches the astrocytes, IP3 is released. IP3 is assumed to be dependent on the amount of 2-AG [19]. This process can be described by

$$\frac{dIP_3}{dt} = (IP_3^* - IP_3)/\tau_{IP3} + r_{IP3}AG, \tag{3}$$

where *IP3* represents the quantity of IP3 in the cytoplasm and r_{IP3} and τ_{IP3} are the production and decay rate of IP3, respectively. *IP3** is a constant. Subsequently, the released 2-AG triggers DSE and eSP through direct and indirect feedback. The relationship between 2-AG and DSE is assumed to be linear [22]:

$$DSE = AG \times K_{AG},\qquad(4)$$

where K_{AG} is the scaling constant. The remaining 2-AG binds to the receptors on astrocytes and then triggers calcium waves inside the astrocytes.

The Li–Rinzel model was utilized to describe the Ca^{2+} dynamics in astrocytes, which is provided as follows [30]:

$$\frac{dCa^{2+}}{dt} = J_{chan}\left(Ca^{2+}, h, IP_3\right) + J_{leak}\left(Ca^{2+}\right) - J_{panp}\left(Ca^{2+}\right).\qquad(5)$$

It can be seen that the Ca^{2+} concentration in astrocytes is regulated by three variables: J_{chan}, J_{leak}, and J_{chan}. J_{chan} is the released Ca^{2+} based on the concentrations of Ca^{2+} and *IP3*, J_{pump} is the amount of Ca^{2+} pumped into the ER, J_{leak} is the leaked Ca^{2+} from the ER, and h is considered to be the fraction of activated IP3Rs. Further details of this model are not repeated here.

The calcium dynamic inside the astrocytes regulates the release of glutamate and then drives *eSP*; it can be described by [22]

$$\begin{aligned} d(Glu)/dt &= -Glu/\tau_{Glu} + r_{Glu}\delta(t - t_{Ca^{2+}}) \\ t_{eSP}d(eSP)/dt &= -eSP + m_{eSP}Glu(t), \end{aligned}\qquad(6)$$

where *Glu* is the amount of glutamate; τ_{Glu} and r_{Glu} are the decay and release rate of glutamate, respectively; $t_{Ca}{}^{2+}$ is the threshold-crossing time of calcium ions; τ_{eSP} is the decay rate of *eSP*; and m_{eSP} is set to a constant in the simulation.

3.3. Bio-Inspired Self-Repairing CPG Model (BiSRP-CPG)

For the convenience of the following research, we used LP and PD neurons located in the crustacean pyloric CPG to distinguish two K-K neurons [31]. The fragment is used to illustrate the BiSRP-CPG model mediated by astrocytes, as presented in Figure 2. This fragment includes an astrocyte (A) and a minimal CPG coupled with two K-K neurons. Each neuron is connected via chemical inhibitory synapses. To demonstrate the self-repairing mechanism, two different network cases were designed. Figure 2a shows a healthy network. Under the stimulation of external synaptic inputs, 2-AG signals are released from LP and PD neurons, generating the DSE and eSP signals via direct and indirect feedback pathways. The balance of these two signals achieves a stable state for the transmission PR. Figure 2b shows a faulty network, where faults occur at partial synapses associated with neuron LP. Consequently, the balance between the DSE and eSP of the LP neuron is disrupted, resulting in an imbalance of PR at the synapses. However, when synapses are broken, the astrocyte can increase the PR value of other healthy synapses connected with neuron LP through indirect feedback, so that the PR value can return to a stable state.

3.4. Excitatory Synaptic Activation

The BiSRP-CPG model is a network consisting of only two neurons; however, neurons cannot exist in isolation in the real physiological environment. The K-K neurons in the CPG are undoubtedly influenced by other neurons. In order to construct a state similar to the real physiological environment, we applied 10 external synapses to the K-K neuron model and employed a Poisson-distributed spike train with an average firing rate of 10 Hz as the action potential. A probability-based model was employed [22,28]:

$$I^i_{syn}(t) = \begin{cases} I_{inj}, range \ \leq PR \\ 0, range > PR. \end{cases}\qquad(7)$$

When there is no fault in BiSRP-CPG, the synaptic transmission probability of release (*PR*) is determined by DSE and eSP.

$$PR(\text{t}) = \left(\frac{PR(\text{t}_0)}{100} \times \text{DSE}(\text{t}) \right) + \left(\frac{PR(\text{t}_0)}{100} \times eSP(\text{t}) \right), \quad (8)$$

where $PR(t_0)$ is the initial *PR* of each synapse. When a fault is injected to the synapse, $PR(t_0)$ is set to the fault value. Please see the Appendix A for specific parameters.
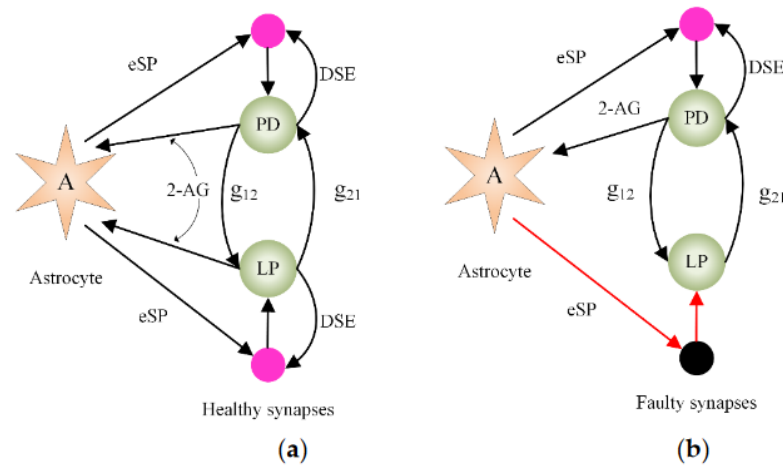
Figure 2. The BiSRP-CPG model. (**a**) Healthy network; (**b**) Faulty network.

4. Simulation of BiSRP-CPG Model

4.1. Robustness against Stochastic Synapses

In this section, how astrocytes enhance the stability of the CPG network is demonstrated. Figure 3 shows the CPG model fragments in the case of different states, including the original ideal minimum CPG neuron network without external stimulation (see Figure 3a), the minimal CPG network without astrocytes under external random stimulation (see Figure 3b), and the BiSRP-CPG network with external random stimulation (see Figure 3c). Moreover, the time series of the membrane potential corresponding to different frame diagrams are also given in Figure 3. The red parts represent neuron LP and the blue parts represent neuron PD. The bursting activities of the CPG were studied via comparison of the membrane potential time series.

The bursting activities without astrocytes was unstable when the interference of external random inputs occurred, while the BiSRP-CPG under the regulation of astrocytes could still generate relatively stable mutually rhythmic bursting waves. The histograms of the inter-cluster duration of the output membrane potentials were plotted (Figure 3) to estimate the stability of the output rhythm. The output rhythm of the ideal CPG without input was completely stable, while the output rhythm of the CPG under random input fluctuated. It can be concluded from the comparison between Figure 3b and 3c that under the regulation of astrocytes, the variation of the length between clusters is smaller than that without astrocytes. That is, the output of astrocyte-mediated BiSRP-CPG is more stable.

For further quantitative analysis of robustness, we extracted the length of the clusters, the number of spikes in clusters, and the length between clusters from the bursting waves of the CPG network with or without astrocytes. The probability density function (PDF) and standard deviation of these three sets of variables were calculated to quantify the experimental results. The experiment results are shown in Figure 4, which indicate that the data in the presence of astrocytes are more stable than that in the absence of astrocytes. The output rhythm of the BiSRP-CPG model demonstrates better performance against external random signal influence than that without astrocytes.
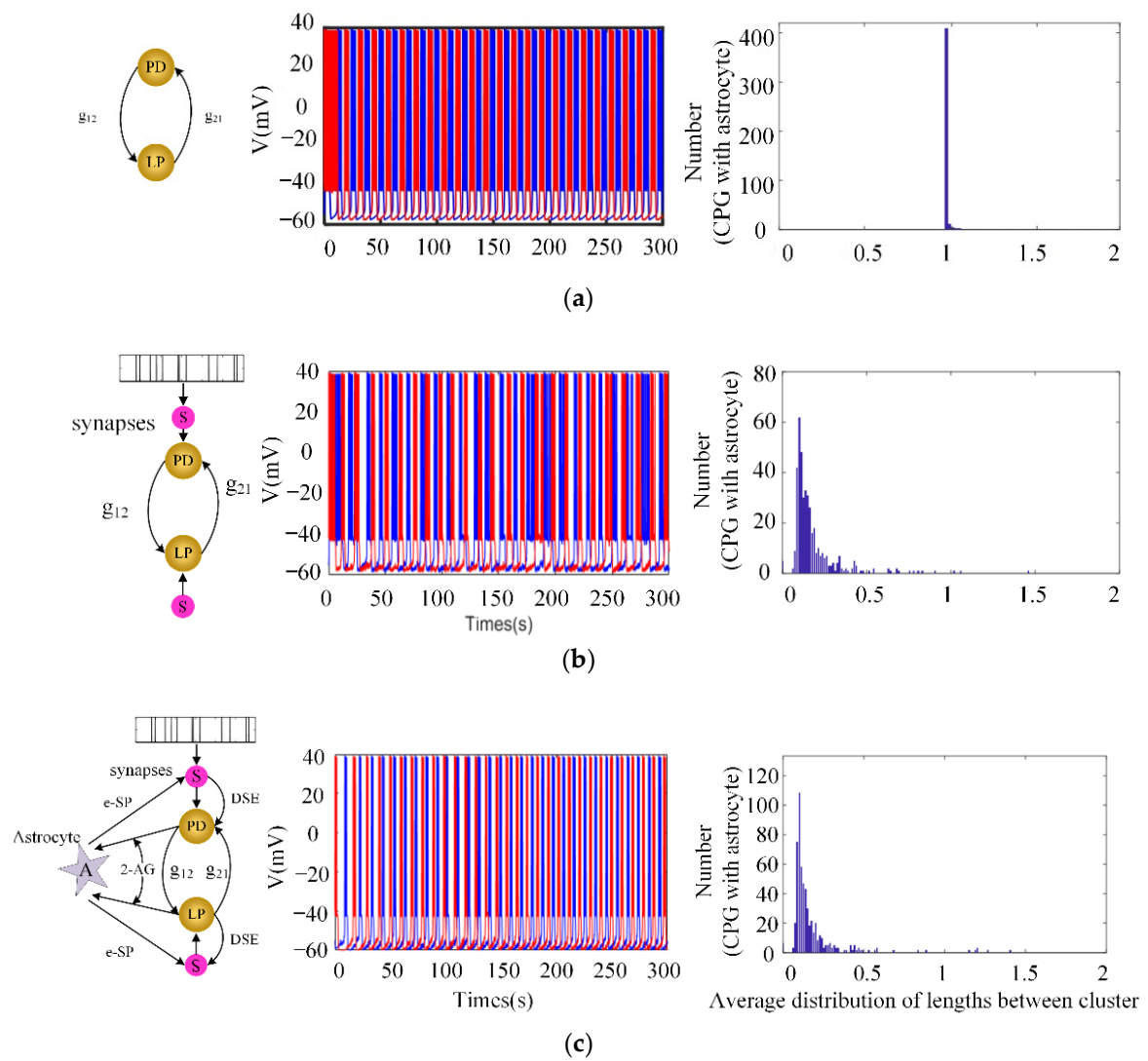
Figure 3. The time series of membrane potentials and frequency histograms of inter-cluster length of (**a**) the ideal minimum CPG neuron network without external stimulation, (**b**) the minimal CPG network in the absence of astrocytes and with external random stimulation, and (**c**) the BiSRP-CPG network with external random stimulation.
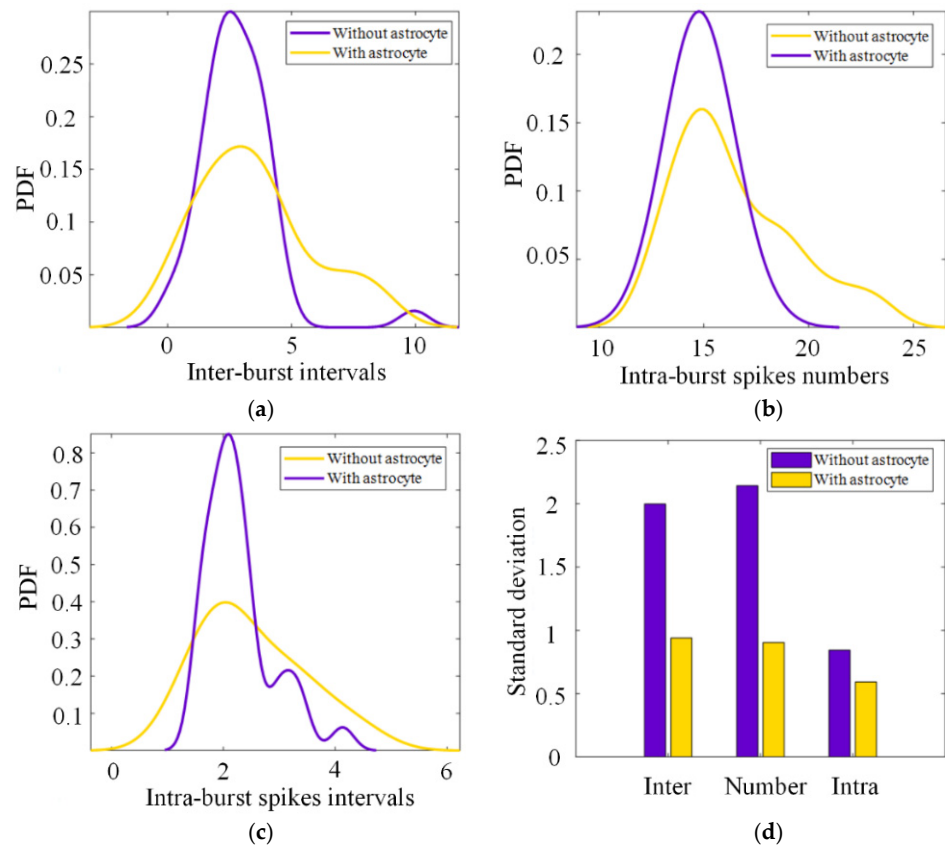
Figure 4. Probability density function and variance statistics of the output of CPG with or without astrocytes. (**a**) The probability density function of the inter-burst intervals; (**b**) The probability density function of the intra-burst spikes numbers; (**c**) The probability density function of the intra-burst spikes intervals; (**d**) Variance statistics of the inter-burst intervals, the intra-burst spikes numbers, and the intra-burst spikes intervals.

4.2. Self-Repair in Case of Fault Synapses

To evaluate the self-repairing capability of BiSRP-CPG, the following two cases were analyzed: First, when the synapses connected to both neurons encountered the same degree of synaptic failures, the output rhythms of BiSRP-CPG and the original CPG were compared. Second, when one neuron in the CPG suffered from different densities of synaptic failure, the dynamic behaviors of the synapses was analyzed to quantify the results of performance degradation analysis of BiSRP-CPG and the original CPG.

In the first experiment, the synaptic PR fault densities of both the LP and PD neurons were set to 20% to demonstrate the self-repair capability, which means each of the two neurons are connected to eight healthy external synapses. It is clear from the comparison of membrane potentials in Figure 5a,b that the BiSRP-CPG model has certain self-repairing capability when synaptic failure occurs. When the synapses attached to the two neurons suffered a 20% loss, the rhythm of the CPG without astrocytes was reduced, and this loss cannot be recovered. However, in the case of BiSRP-CPG regulated by astrocytes, the bursting rhythms can gradually return to the normal level. The failure rates for the two cases were further calculated, showing that when the synaptic failure rate is 20%, the average spiking loss rate of the CPG network without astrocytes is 36.84%, while the spiking loss rate of BiSRP-CPG is only 10.53%. This means that the astrocyte-mediated CPG model only had 10.53% performance degradation when both neurons suffered a synaptic fault density of 20%, which further proves that astrocytes play a key role in the stability of the CPG rhythm.
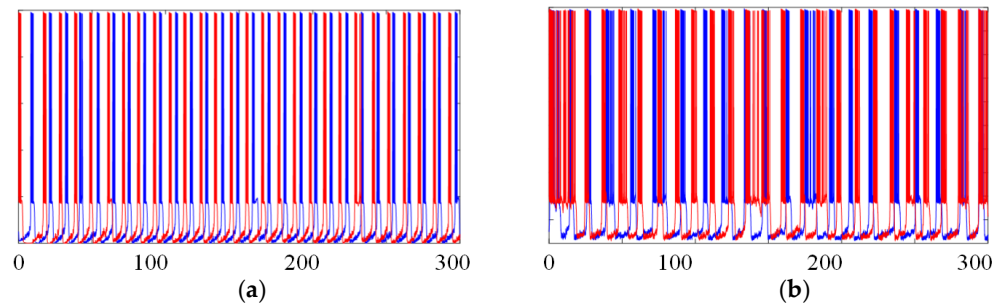
Figure 5. (**a**) The membrane potentials of the BiSRP-CPG network; (**b**) The membrane potentials of the original CPG network without astrocytes. Both neurons suffered a synaptic fault density of 20%.

In addition, the dynamic behaviors of synapses connected with the CPG neurons were analyzed when the neuron LP (red parts) encountered different synaptic fault densities. The results are presented in Figure 6, including the membrane potentials of the neurons in BiSRP-CPG, the PRs of healthy synapse connected to the LP and PD neurons, DSE signals, and eSP signals. The range of the healthy PR and DSE signals under different fault densities are marked in each panel. Obviously, when a fault occurs in the LP neuron (red parts), the eSP signals of both neurons remained unchanged at different synaptic fault densities, but the absolute value range of the synaptic DSE gradually decreased with increasing synaptic fault density. This is because the PR value of a synapse is the summation of eSP and DSE. When the neuron LP encounters a synaptic failure, the entire CPG system falls into an unbalanced state. The eSP signal from astrocytes compensated for system loss by increasing the PR value of the remaining healthy synapses. For example, when the synaptic fault density of neuron LP is 30%, the enhanced PR value of healthy synapse is 0.3~1; when the fault density is 40%, the PR value is enhanced to 0.5~1.2. This means that the remaining healthy synapses have a greater chance of transmitting spikes to the postsynaptic neuron, which endows BiSRP-CPG with self-repairing capability at high fault densities.

In order to quantify the loss rates of the CPG system with and without astrocytes under different synaptic fault densities, the CPG output failure rate (*FR*) with or without astrocytes was calculated and compared according to the following formula:

$$FR = \frac{N_t - N_a}{N_t}, \tag{9}$$

where N_a represents the actual number of clusters of CPG with partial synaptic fault and N_t represents the total number of clusters of CPG with no fault under the same conditions. The statistical results of the failure rates (*FR*) of the CPG with or without astrocytes at different synaptic fault densities are shown in Figure 7. It is clear that the failure rate of BiSRP-CPG is always lower than that without astrocytes as the synaptic fault density increases. When synaptic failure density reaches more than 60%, most synapses are broken and CPG cannot produce rhythmic output. Thus, *FR* increases to 100%. In summary, with the feedback of astrocytes, neurons in BiSRP-CPG can sense failures within a certain range and implement repair actions to maintain the stability of the CPG system.
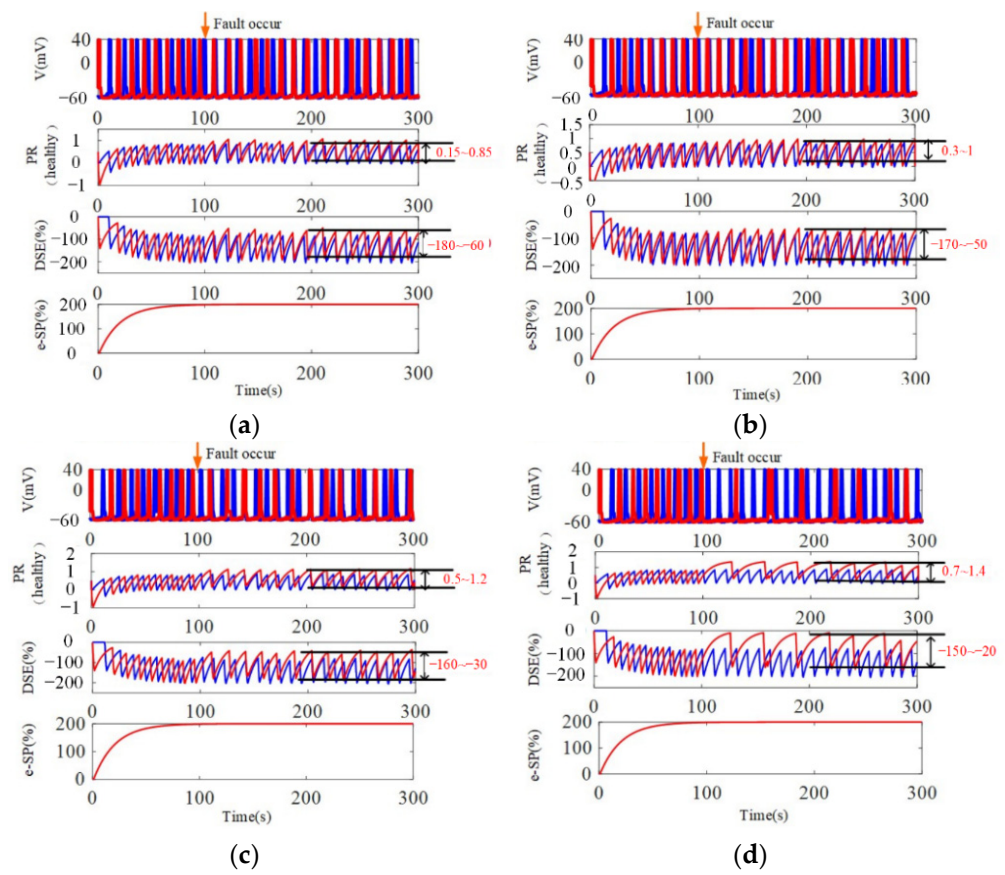
Figure 6. The dynamic behaviors of synapses connected with the CPG neurons when the neuron LP encountered synaptic failure at 100 s. The red parts indicate the neuron LP, and the blue parts indicate the neuron PD with no fault. The fault densities include (**a**) 20%, (**b**) 30%, (**c**) 40%, and (**d**) 50%. Each figure includes the member potentials of the astrocyte-mediated BiSRP-CPG, the PR of healthy synapses connected to neuron LP and neuron PD, DSE signal, and eSP signal.
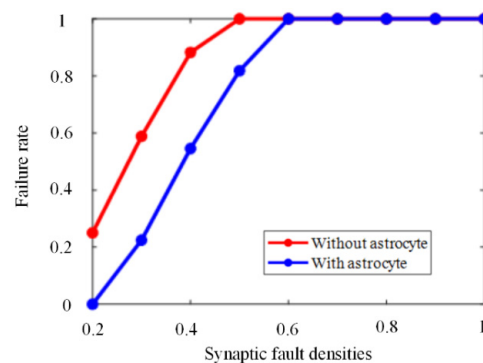
Figure 7. Failure rates at different synaptic fault densities.

5. FPGA Realization of BiSRP-CPG

5.1. Hardware Architecture

Based on the above simulation results, the hardware implementation of BiSRP-CPG was further carried out on FPGA. Our aim was to introduce the self-repairing mechanism into a hardware system, perform simulation with a real-time scale, and further demonstrate the potential of BiSRP-CPG in practical applications. In the implementation process, each model was discretized to realize parallel pipeline calculation. In order to reduce the hardware resource consumption and computational complexity, the multipliers were replaced by logical shift and addition. The idea of this method is to transform the constant

term in multiplication into a power of base 2. In this way, the shift operations can be realized by the logical shifters first, and then the corresponding addition and subtraction operations are performed according to the desired result. Figures 8–10 respectively show the neuron model variable pipeline calculation structure, the ionic current variable pipeline calculation structure, and the tripartite synaptic variable pipeline calculation structure. The structure details of the pipeline are given in the figures. The green blocks represent different logic operations, and the arrows represent the data flow and shift operations in the channel.
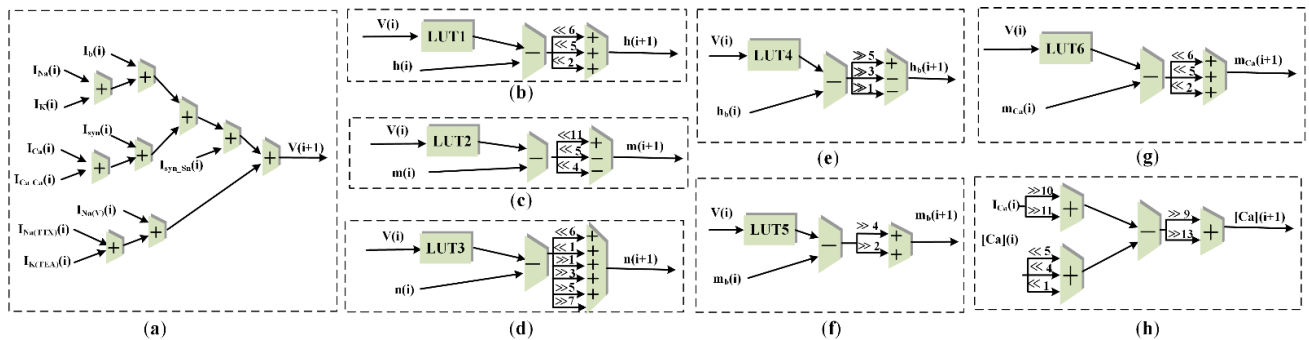
Figure 8. Neuron model variable pipeline calculation structure, containing (**a**) the membrane potential (V) pipeline and (**b**–**h**) seven variable pipelines (h, m, n, h_b, m_b, m_{Ca}, and [Ca²⁺]), respectively updating the eight variables in the K-K neuron model. I_{syn} and I_{syn_sn} are the chemical synaptic current and the external random synaptic current injected into the neuron, respectively.
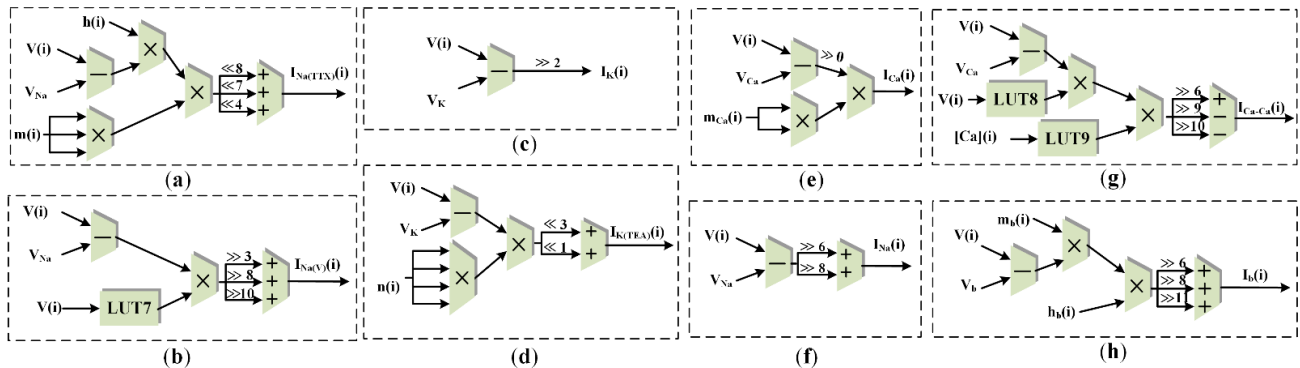
Figure 9. Ionic current variable pipeline calculation structure. Each channel calculates one ionic current in the K-K neuron model separately: (**a**) TTX-sensitive sodium current ($I_{Na(TTX)}$), (**b**) the stationary voltage-dependent sodium current ($I_{Na(V)}$), (**c**) the leaky sodium current (I_K), (**d**) the TEA-sensitive potassium current ($I_{E(TEA)}$), (**e**) the leaky potassium current (I_{Ca}), (**f**) the inward calcium current (I_{Na}), (**g**) the stationary voltage-dependent calcium current ($I_{Ca\text{-}Ca}$), and (**h**) the voltage-dependent outward current (I_b).
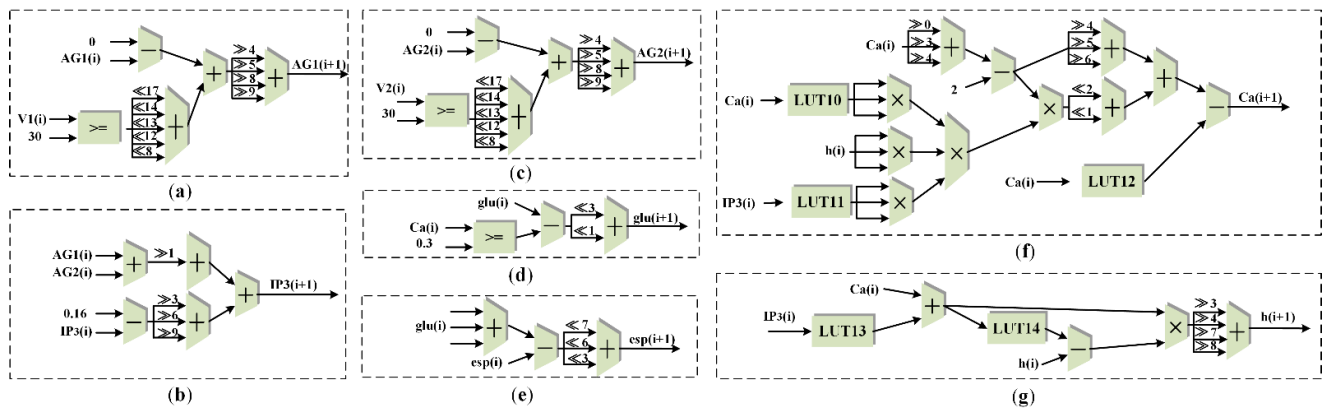
Figure 10. Tripartite synapse variable pipeline calculation structure, containing (**a**,**c**) 2-AG pipeline, (**b**) IP3 pipeline, (**d**) glu pipeline, (**e**) esp pipeline, (**f**) Ca pipeline, and (**g**) h pipeline. V1(i) and V2(i) are the membrane potentials of PD and LP neurons at time i, respectively.

The function of the neuron model variable pipeline calculation structure is to calculate and update the value of the neuron membrane potential. According to the K-K neuron model, currents being injected by the synapses causes the change of membrane potentials and generates action potentials. Eight conductance-based ionic currents in K-K neurons and currents injected by synapses were utilized as input signals, which came from the ionic current pipeline calculation structure and the synaptic structure, respectively. The continuous differential equation was discretized using the Euler method. Note that a reasonable time step can reduce the error caused by the discretization and improve the simulation accuracy; hence, the time step in this article was set as Δt = 0.00005 s. As shown in Figure 8, the current values of the membrane potential (V) and the other seven variables (h, m, n, h_b, m_b, m_{Ca}, and [Ca^{2+}]) were calculated through eight pipelines. Each pipeline was set up with a dedicated buffer to store the variable value in the corresponding variable register block. These variables were buffered and input to other pipelines for the next iteration at each time step. If the membrane potential is greater than the threshold V_{th}, a spike will be generated. In addition, all pipelines require only a small number of multipliers, which greatly saves hardware resource consumption. Taking the h variable pipeline in Figure 8b as an example, the exponential decay of the membrane potential V at time i can be calculated using a look-up table (LUT). Traditional methods multiply the result directly by a scaling factor. However, we rewrote the scale factor 0.01 in the multiplication operation as $1/(2^6 + 2^5 + 2^2)$ to realize the multiplier-free neural variable operation.

Similarly, the structure of the ionic current variable pipeline is shown in Figure 9. This structure contains eight pipelines to calculate the eight physiological significant ionic current values in the K-K model.

Figure 10 shows the tripartite synapse variable pipeline calculation structure, which implements the direct and indirect feedback pathways in tripartite synapses. When the spike train generated by the random number generator reaches the pipeline, the LP and PD neurons respectively update AG (see Figure 10a,c). Under the stimulation of 2-AG, astrocytes produce IP3 (see Figure 10b). Subsequently, calcium ions are released through three channels: J_{chan}, J_{pump}, and J_{leak} (see Figure 10f). The input signals of the calcium ion pipeline are related to $Ca2+$, h, and $IP3$ stored in the corresponding variable registers. Similarly, the values of Glu and eSP are calculated and updated in the pipeline shown in Figure 10d,e.

The overall hardware structure of BiSRP-CPG based on FPGA is shown in Figure 11. The whole system consists of a CPG module and an astrocyte module. The CPG module contains a pair of K-K neurons connected to each other through inhibitory synapses. Each neuron maintains a set of neural variables that update membrane potentials in real time.

The astrocyte module receives AG signals from CPG modules and generates eSP signals to carry out indirect feedback. In this paper, the self-repairing of CPG networks by astrocytes is implemented through hardware circuits. The repair of this CPG network can be analyzed by setting different failure rates of the external synapses.
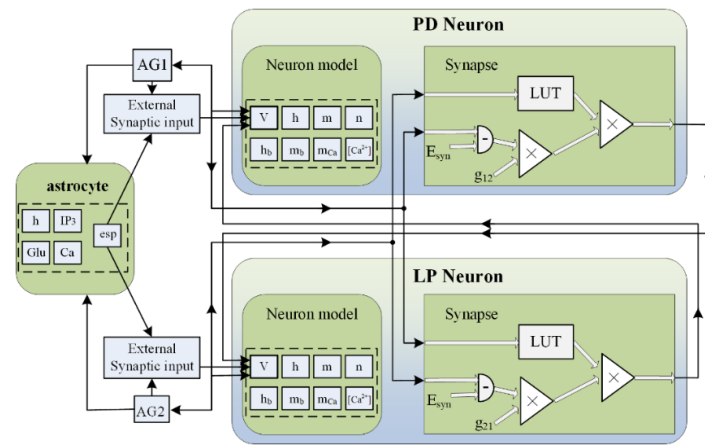
Figure 11. Overall hardware structure of BiSRP-CPG based on FPGA. LP and PD neurons connect with each other through inhibitory synapses. The external synaptic inputs are modulated by both AG signals and the eSP signal from astrocytes for both direct and indirect feedback.

5.2. Experimental Results

Figure 12a shows the FPGA hardware system platform. Figure 12b,c shows the CPG output waveforms under the fault condition mentioned in Section 4 (i.e., only the LP neuron encounters synaptic loss at different failure rates), in which the discharge behaviors of the BiSRP-CPG network under different synaptic failure rates are compared with that of original CPG network. The results show that the CPG output waveforms at different synaptic failure rates are consistent with the software simulation results. It can be demonstrated that when random synapses and fault synapses are introduced, BiSRP-CPG networks are more robust and self-repairing compared to the state without astrocytes.
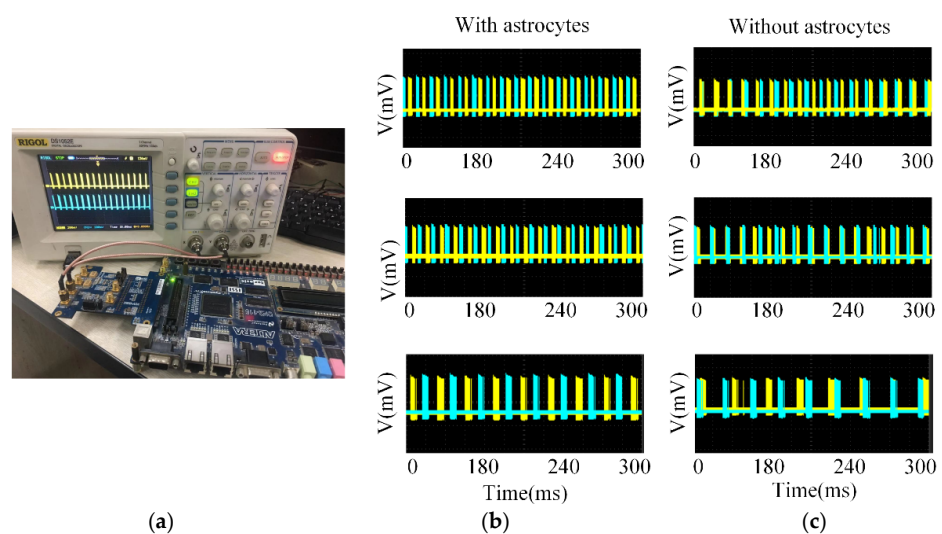
Figure 12. Hardware implementation results of self-repairing CPG network. (**a**) Hardware used in the experiment; (**b**) The discharge time series of BiSRP-CPG; (**c**) The discharge time series of the CPG model without astrocytes. The discharge loss rates from top to bottom are 20%, 30%, and 40%.

Figure 13 shows the healthy synaptic PR values and DSE waveforms at different failure rates. The fluctuation ranges of PR and DSE signals are labeled in the figures. The comparison results show that with the increase in synaptic failure rate, the absolute values of DSE signals gradually decrease, resulting in a gradual increase in the PR values, which is consistent with the software simulation results of BiSRP-CPG. Thus, it is further demonstrated that the self-repairing modulation of astrocytes for healthy synapses can be migrated to the FPGA platform, with better real-time performance and faster simulating.
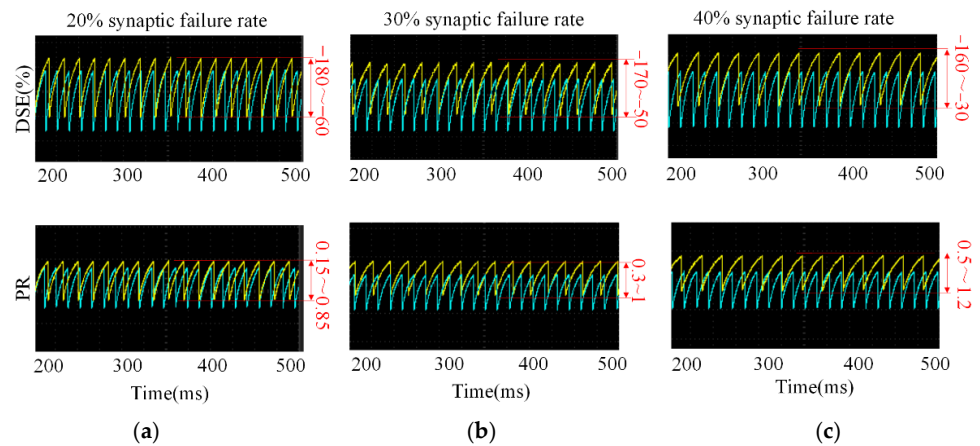
Figure 13. PR values and DSE signals at different failure rates, respectively: (**a**) 20% synaptic failure rate; (**b**) 30% synaptic failure rate; (**c**) 40% synaptic failure rate.

Table 1 lists the resource utilization checklists for the multiplier-free hardware implementation proposed in this paper and the traditional multiplier implementation. It is clearly indicated that the multiplier-free implementation method greatly reduces resource consumption, especially the total logic resources and embedded multipliers. Therefore, the method without multipliers can provide a solution for the case of achieving a larger network structure with fewer hardware resources.

Table 1. List of hardware implementation resource utilization.

FPGA Resource Type	Total Logical Resource	Traditional Implementation	Multiplier-Free Implementation
Total logical resource	114,480	70,560 (210%)	23,101 (20%)
Dedicated logical register	114,480	5980 (2%)	2118 (2%)
Pin	529	34 (6%)	34 (6%)
Block RAM resource (bit)	3,981,312	8,251,559 (140%)	3,057,664 (77%)
Embedded multiplier	532	2058 (459%)	501 (94%)
Phase-locked loop circuit	4	1	1

6. Discussion

A hypothesis from the physiological significance is proposed in this paper: that an astrocyte-mediated environment is one of the key factors for the CPG network to maintain relative stability under external interference. This study is primarily aimed at understanding how CPG in an astrocyte environment regulates its own stability in response to random external stimulation or injuries. We presented a new astrocyte-mediated CPG network model, the BiSRP-CPG, which relies on endogenous cannabinoid interactions between astrocytes and CPG neurons. An FPGA-based hardware simulation platform was used to evaluate the robustness and self-repairing capabilities of the network. The pipeline strategy and a multiplier-free implementation method were utilized to reduce the

hardware overhead of BiSRP-CPG system. The experiment results demonstrate that this indirect feedback from astrocytes can enhance the robustness of the system when CPG is subjected to external random stimulation, and can exert a certain self-repairing capability when synaptic failure occurs. The proposed BiSRP-CPG based on the tripartite synapse opens up a new path for understanding the mechanisms that support the robustness and fine-grained repair capabilities of the CPG system.

However, there are still many problems worthy of further study, mainly in the following aspects:

(1) A more comprehensive study of the relationship between system-related dynamics and model parameters is needed to better understand how each parameter affects the dynamic behaviors of the astrocyte-mediated CPG internal neurons and the overall CPG network.

(2) The self-repairing ability of BiSRP-CPG should be applied to the fault-tolerant algorithm of electronic system. System reliability should be provided for hardware systems and large-scale equipment through autonomous perception and repair of faults (such as environmental changes and signal loss) [32].

(3) The BiSRP-CPG should be applied to the controller for bio-inspired robot applications. This novel CPG system should be combined with brain machine interface (BMI) technology for exercise rehabilitation [33].

Author Contributions: Methodology, writing—original draft preparation, writing—review and editing, J.X.; validation, investigation, M.L. and Z.Z.; supervision, project administration, funding acquisition, X.W. All authors have read and agreed to the published version of the manuscript.

Institutional Review Board Statement: Not applicable.

Informed Consent Statement: Not applicable.

Data Availability Statement: Not applicable.

Conflicts of Interest: The authors declare no conflict of interest.

Appendix A

Table A1. Parameter values for the neuron model.

Parameter	Value	Parameter	Value
C_m	0.02 μF	R	0.1 mm
V_{Na}	40 mV	k_s	50 s−1
V_k	−70 mV	ρ	0.002
V_b	−58 mV	k_β	15,000 mM−1
V_{Ca}	150 mV	β	0.00004
$g_{Na(TTX)}$	400 μS	$g_{Na(V)}$	0.13 μS
g_{Na}	0.02 μS	$g_{K(TEA)}$	10 μS
g_K	0.25 μS	g_b	0.18 μS
g_{Ca}	1 μS	g_{Ca_Ca}	0.015 μS
E_{syn}	−65 mV	V_{fast}	44.7 mV

Table A2. Parameter values for the astrocyte–neuron model.

Parameter	Value	Parameter	Value
IP_3^*	0.16 μM	k_{ER}	0.1 μM
r_{IP3}	0.5 μMs^{-1}	d_1	0.13 μM
τ_{IP3}	7 s	d_2	1.049 μM
τ_{AG}	10 s	d_3	0.9434 μM
τ_{Glu}	100 ms	d_5	0.08234 μM
eSP	40 S	C_0	2 μM
r_L	0.11 s^{-1}	C_1	0.185
r_c	6 s^{-1}	a_0	0.2 μMs^{-1}
r_{Glu}	10 μMs^{-1}	m_{eSP}	55×10^3
v_{ER}	0.8 μMs^{-1}	Ca^{2+} threshold	0.3 μM

Table A3. Initial variables for the astrocyte model.

Variables	Value	Variables	Value
Ca^{2+}	0.071006 μM	n_∞	0
h	0.7791	m_∞	0
J_{chan}	0	AG	0
J_{leak}	0	eSP	0
J_{pump}	0	IP_3	0.16 μM

References

1. Weaver, A.L.; Roffman, R.C.; Norris, B.J.; Calabrese, R.L.; Kristan, W. A Role for Compromise: Synaptic Inhibition and Electrical Coupling Interact to Control Phasing in the Leech Heartbeat CPG. *Front. Behav. Neurosci.* **2010**, *4*, 1–17. [CrossRef] [PubMed]
2. Dickinson, P.S. Neuromodulation of Central Pattern Generators in Invertebrates and Vertebrates. *Curr. Opin. Neurobiol.* **2006**, *16*, 604–614. [CrossRef] [PubMed]
3. Martínez-Silva, L.; Manjarrez, E.; Gutiérrez-Ospina, G.; Quevedo, J.N. Electrophysiological Representation of Scratching CPG Activity in the Cerebellum. *PLoS ONE* **2014**, *9*, e109936. [CrossRef] [PubMed]
4. Lafreniere-Roula, M.; McCrea, D.A. Deletions of Rhythmic Motoneuron Activity during Fictive Locomotion and Scratch Provide Clues to the Organization of the Mammalian Central Pattern Generator. *J. Neurophysiol.* **2005**, *94*, 1120–1132. [CrossRef] [PubMed]
5. Minassian, K.; Hofstoetter, U.S.; Dzeladini, F.; Guertin, P.A.; Ijspeert, A. The Human Central Pattern Generator for Locomotion: Does It Exist and Contribute to Walking? *Neuroscientist* **2017**, *23*, 649–663. [CrossRef]
6. Grillner, S.; El Manira, A. Current Principles of Motor Control, with Special Reference to Vertebrate Locomotion. *Physiol. Rev.* **2020**, *100*, 271–320. [CrossRef]
7. Zhong, G.; Shevtsova, N.A.; Rybak, I.A.; Harris-Warrick, R.M. Neuronal Activity in the Isolated Mouse Spinal Cord during Spontaneous Deletions in Fictive Locomotion: Insights into Locomotor Central Pattern Generator Organization. *J. Physiol.* **2012**, *590*, 4735–4759. [CrossRef]
8. Tavoosi, J.; Shirkhani, M.; Abdali, A.; Mohammadzadeh, A.; Nazari, M.; Mobayen, S.; Asad, J.H.; Bartoszewicz, A. A New General Type-2 Fuzzy Predictive Scheme for PID Tuning. *Appl. Sci.* **2021**, *11*, 10392. [CrossRef]
9. Huang, H.; Shirkhani, M.; Tavoosi, J.; Mahmoud, O. A New Intelligent Dynamic Control Method for a Class of Stochastic Nonlinear Systems. *Mathematics* **2022**, *10*, 1406. [CrossRef]
10. Cao, Y.; Lu, Y.; Cai, Y.; Bi, S.; Pan, G. CPG-Fuzzy-Based Control of a Cownose-Ray-like Fish Robot. *Ind. Rob.* **2019**, *46*, 779–791. [CrossRef]
11. Cao, Y.; Xie, Y.; He, Y.; Pan, G.; Huang, Q.; Cao, Y. Bioinspired Central Pattern Generator and T-S Fuzzy Neural Network-Based Control of a Robotic Manta for Depth and Heading Tracking. *J. Mar. Sci. Eng.* **2022**, *10*, 758. [CrossRef]
12. Bushong, E.A.; Martone, M.E.; Jones, Y.Z.; Ellisman, M.H. Protoplasmic Astrocytes in CA1 Stratum Radiatum Occupy Separate Anatomical Domains. *J. Neurosci.* **2002**, *22*, 183–192. [CrossRef]
13. Clarke, L.E.; Barres, B.A. Emerging Roles of Astrocytes in Neural Circuit Development. *Nat. Rev. Neurosci.* **2013**, *14*, 311–321. [CrossRef]
14. Stevens, B. Neuron-Astrocyte Signaling in the Development and Plasticity of Neural Circuits. *NeuroSignals* **2008**, *16*, 278–288. [CrossRef]
15. De Pittà, M.; Brunel, N.; Volterra, A. Astrocytes: Orchestrating Synaptic Plasticity? *Neuroscience* **2016**, *323*, 43–61. [CrossRef]
16. Li, K.; Li, J.; Zheng, J.; Qin, S. Reactive Astrocytes in Neurodegenerative Diseases. *Aging Dis.* **2019**, *10*, 664. [CrossRef]
17. Allen, N.J.; Eroglu, C. Cell Biology of Astrocyte-Synapse Interactions. *Neuron* **2017**, *96*, 697–708. [CrossRef]
18. Kwon, H.S.; Koh, S.H. Neuroinflammation in Neurodegenerative Disorders: The Roles of Microglia and Astrocytes. *Transl. Neurodegener.* **2020**, *9*, 42. [CrossRef]

19. Volman, V.; Ben-Jacob, E.; Levine, H. The Astrocyte as a Gatekeeper of Synaptic Information Transfer. *Neural. Comput.* **2007**, *19*, 303–326. [CrossRef]

20. Wade, J.J.; McDaid, L.J.; Harkin, J.; Crunelli, V.; Kelso, J.A.S.; Beiu, V. Exploring retrograde signaling via astrocytes as a mechanism for self repair. In Proceedings of the International Joint Conference on Neural Networks, San Jose, CA, USA, 31 July–5 August 2011.

21. Komendantov, A.O.; Kononenko, N.I. Deterministic Chaos in Mathematical Model of Pacemaker Activity in Bursting Neurons of Snail, Helix Pomatia. *J. Theor. Biol.* **1996**, *183*, 219–230. [CrossRef]

22. Wade, J.; McDaid, L.; Harkin, J.; Crunelli, V.; Kelso, S. Self-Repair in a Bidirectionally Coupled Astrocyte-Neuron (AN) System Based on Retrograde Signaling. *Front. Comput. Neurosci.* **2012**, *6*, 76. [CrossRef]

23. Halassa, M.M.; Fellin, T.; Takano, H.; Dong, J.H.; Haydon, P.G. Synaptic Islands Defined by the Territory of a Single Astrocyte. *J. Neurosci.* **2007**, *27*, 6473–6477. [CrossRef]

24. Araque, A.; Parpura, V.; Sanzgiri, R.P.; Haydon, P.G. Tripartite Synapses: Glia, the Unacknowledged Partner. *Trends Neurosci.* **1999**, *22*, 208–215. [CrossRef]

25. Alger, B.E. Retrograde Signaling in the Regulation of Synaptic Transmission: Focus on Endocannabinoids. *Prog. Neurobiol.* **2002**, *68*, 247–286. [CrossRef]

26. Marchant, J.; Callamaras, N.; Parker, I. Initiation of IP3-Mediated Ca2+ Waves in Xenopus Oocytes. *EMBO J.* **1999**, *18*, 5285–5299. [CrossRef]

27. Navarrete, M.; Araque, A. Endocannabinoids Potentiate Synaptic Transmission through Stimulation of Astrocytes. *Neuron* **2010**, *68*, 113–126. [CrossRef]

28. Liu, J.; Harkin, J.; Maguire, L.P.; McDaid, L.J.; Wade, J.J. SPANNER: A Self-Repairing Spiking Neural Network Hardware Architecture. *IEEE Trans. Neural Netw. Learn. Syst.* **2018**, *29*, 1287–1300. [CrossRef]

29. Golowasch, J.; Casey, M.; Abbott, L.F.; Marder, E. Network Stability from Activity-Dependent Regulation of Neuronal Conductances. *Neural Comput.* **1999**, *11*, 1079–1096. [CrossRef]

30. Li, Y.X.; Rinzel, J. Equations for InsP3 Receptor-Mediated [Ca2+](i) Oscillations Derived from a Detailed Kinetic Model: A Hodgkin-Huxley like Formalism. *J. Theor. Biol.* **1994**, *166*, 461–473. [CrossRef]

31. Doloc-Mihu, A.; Calabrese, R.L. A Database of Computational Models of a Half-Center Oscillator for Analyzing How Neuronal Parameters Influence Network Activity. *J. Biol. Phys.* **2011**, *37*, 263–283. [CrossRef]

32. Gantel, L.; Berthet, Q.; Amri, E.; Karlov, A.; Upegui, A. Fault-Tolerant FPGA-Based Nanosatellite Balancing High-Performance and Safety for Cryptography Application. *Electronics* **2021**, *10*, 2148. [CrossRef]

33. Saggese, G.; Strollo, A.G.M. A Low Power 1024-Channels Spike Detector Using Latch-Based RAM for Real-Time Brain Silicon Interfaces. *Electronics* **2021**, *10*, 3068. [CrossRef]